IOP Publishing Plasma Sources Science and Technology
Plasma Sources Sci. Technol. **34** (2025) 015009 (11pp) https://doi.org/10.1088/1361-6595/ada8d8

The quenching effect of oxygen addition on an argon capacitively coupled plasma: experimental and computational study of the argon metastable atom kinetics

Lan-Yue Luo[1], Zoltán Donkó[2], Ranna Masheyeva[2], Máté Vass[2,3], He-Ping Li[1,*] and Peter Hartmann[2,*]

[1] Department of Engineering Physics, Tsinghua University, Beijing 100084, People's Republic of China
[2] Institute for Solid State Physics and Optics, HUN-REN Wigner Research Centre for Physics, Konkoly Thege Miklós str. 29-33, 1121 Budapest, Hungary
[3] Chair of Applied Electrodynamics and Plasma Technology, Faculty of Electrical Engineering and Information Sciences, Ruhr University Bochum, 44801 Bochum, Germany

E-mail: hartmann.peter@wigner.hu and liheping@tsinghua.edu.cn

Received 29 August 2024, revised 3 November 2024
Accepted for publication 10 January 2025
Published 30 January 2025

Abstract

The effect of oxygen admixture in an argon capacitively coupled radio-frequency plasma is investigated experimentally and computationally in a symmetrical discharge cell, at pressures $\leqslant$10 Pa. In the experiments, tunable diode laser absorption spectroscopy is applied to monitor the densities of the Ar $1s_5$ ($\xrightarrow{772.376\,\mathrm{nm}}$ $2p_6$) and $1s_3$ ($\xrightarrow{772.421\,\mathrm{nm}}$ $2p_2$) metastable atoms in the plasma as a function of the oxygen content in the working gas. In order to enhance computational efficiency, the modelling is divided into two steps. First, the electron energy probability function (EEPF) is obtained from a particle-in-cell/Monte Carlo collision simulation of the Ar/O_2 plasma without considering the dynamics of the excited levels of Ar atoms. As the second step, this EEPF is fed into a code that solves the balance equations of Ar atoms in numerous excited levels. These equations comprise the effects of diffusion, direct and stepwise excitation processes, stepwise and pooling ionization, as well as radiative transfer between the various Ar atomic levels, and the quenching of the excited Ar atoms by O_2 molecules. Using this approach is justified by the fact that the EEPF is insensitive to the excited level dynamics at low pressures, as shown in previous studies. The measurements and simulations are found to yield consistent results, indicating the correctness of the literature values of the quenching coefficient of Ar $1s_5$ and $1s_3$ by oxygen molecules.

Keywords: capacitively coupled plasma, quenching of metastable atoms, hybrid plasma simulation

* Authors to whom any correspondence should be addressed.

1. Introduction

Excited atoms/molecules may play an important role in the dynamics of gas discharges, including direct-current and radio-frequency (RF) operation [1–4]. Taking Ar gas as an example, it has been discussed in previous papers, e.g. Roberto *et al* [5], that in addition to the direct ionization caused by electron impact with ground state (GS) Ar atoms, the ionization from indirect channels could also become prominent. These indirect ionization ways include stepwise ionization:

$$e^- + Ar^* \rightarrow Ar^+ + 2e^- \quad (1)$$

and pooling ionization:

$$Ar^* + Ar^* \rightarrow Ar^+ + Ar + e^- \quad (2)$$

where * denotes the excited levels. Despite their mole fraction being a few orders of magnitude smaller compared with that of the GS atoms, the lower energy thresholds of stepwise processes allow for the possibility of a substantial ionization rate. Hence the contribution from stepwise and pooling ionization could surpass that of direct ionization as the pressure increases, as found in experiment [6] and simulation [5].

Recent works indicate a renewed interest in this topic [7–10]. Progress in the field is also made possible by the availability of high-performance computational resources that allow execution of computationally intensive physical models of these plasmas [1, 11, 12].

A lot of effort has been devoted to the study of the kinetics of argon metastable atoms in discharges [13–15]. Our work focuses on capacitively coupled plasmas (CCPs) due to its important role in plasma etching [16], surface deposition [17], and other industrial applications [18]. Commonly in experiments, the non-intrusive method of laser absorption spectroscopy is employed for the measurement of absolute line-averaged metastable densities or density distributions [19, 20]. In most experiments, measurements of the Ar $1s_5$ metastables were targeted, while less information is available about the other metastables, e.g. $1s_3$, which typically have a lower density. (Note that in this paper we use the Paschen notation for the excited Ar levels.) In simulations, the metastable species are mostly treated as a fluid component, while the charged species, including the electrons, can be described either with a fluid model [13], the PIC/MCC (particle-in-cell/Monte Carlo collisions) method [11], or a hybrid combination of both [14]. Although the majority of PIC/MCC models consider only charged particles in their calculations, there has been a growing interest in including excited levels in some extended PIC/MCC models, e.g. the work of Zheng *et al* [12], Sharma *et al* [15] and Wen *et al* [1, 21–23]. The metastable density is obtained by solving a balance equation that incorporates various population and depopulation processes. By means of simulation, it is possible to study certain physical properties that are difficult to detect experimentally, thereby gaining a deeper understanding to the processes involved in discharges. For instance, the relative contributions of the populating and depopulating processes to the metastable density can be compared, as shown in the papers of Bogaerts *et al* [24, 25]. Furthermore, previous studies have demonstrated that the presence of metastable atoms can influence the plasma density [22, 26].

Prior to the analysis of complex simulation results, it is essential to verify whether the simulation method is capable of accurately representing the actual physical characteristics. This is typically accomplished by comparing the modeling results with those obtained from experiments. For example, the collisional-radiative model proposed by Zhu and Pu [27] was validated by the good agreement of the excited level densities from simulation and experiments in different plasma sources under a wide range of pressure. Similarly, for the PIC/MCC approach proposed by Donkó *et al* [11], a comparison was made between the metastable density profiles obtained from the simulation and experiments conducted at various pressures and voltages.

In addition to pure argon, discharges diluted with other gases have also been the subject of considerable interest and research. Extensive research has been conducted into oxygen-containing plasmas [14, 28–32] due to their relevance in plasma processing applications. In Ar/O_2 mixtures, it has been demonstrated that quenching by molecular oxygen could be the most significant loss process of argon metastable atoms. The quenching rate coefficient is so large that even a small amount of oxygen will lead to a rapid decline in metastable density. This conclusion is supported by experimental results [29–31], as well as simulations [14, 32]. Moreover, as one of the unintentional impurity sources in experimental measurements, even a small percentage of oxygen can introduce a significant degree of uncertainty to the density of Ar metastable atoms. It is therefore worthwhile to investigate the quenching mechanism of oxygen to argon metastable atoms. However, a different trend has been observed in inductively coupled plasmas (ICPs), whereby the addition of oxygen has been found to result in an initial increase in metastable densities before a subsequent decline [33–35]. The increase was attributed to the dominance of electron-induced quenching rather than oxygen-induced quenching at low oxygen ratios, as demonstrated by the findings of Hayashi *et al* [34]. The electron density was found to diminish with rising oxygen content, thereby reducing the overall quenching rates for argon metastables and resulting in elevated argon metastable densities.

The present investigation is aimed at systematic measurements of the densities of both Ar metastable species, $1s_5$ and $1s_3$, over a range of gas pressure of 3.5–10 Pa and oxygen content in the gas mixture of 0%–10%, in a geometrically symmetric CCP operated at 13.56 MHz excitation frequency and 60–300 V peak-to-peak RF voltages, at 4 cm electrode gap. The measurements are based on tunable diode laser absorption spectroscopy (TDLAS). The experimental data are compared to modeling results, which are obtained using a PIC/MCC code for the Ar/O_2 RF plasma and a fluid code for the Ar excited species. Section 2 introduces the experimental setup and measurement method, while section 3 describes the employed numerical code. The results of our study are presented and discussed in section 4. Finally, the work is summarized and conclusions are drawn in section 5.

2. Experimental method

2.1. Experimental setup

The $1s_5$ and $1s_3$ metastable densities in the center of the discharge gap are measured experimentally in our 'Budapest v.3' plasma reactor by tunable diode laser absorption spectroscopy method as shown in figure 1. The discharge chamber was introduced in [36, 37]. It is a geometrically symmetric construction within a quartz cylinder. The parallel flat electrodes, made of Type 304 stainless steel with identical diameters of 14.0 cm are positioned inside the chamber facing each other at a distance of 4.0 cm. The upper electrode is subjected to a 13.56 MHz RF voltage with peak-to-peak values ranging from 60 V to 300 V, while the lower electrode is maintained at ground potential. The driving voltage is provided by a waveform generator (Tokyo Hi-Power RF-150) connected to an impedance-matching box (Tokyo Hi-Power MB-300). The voltage is measured with a high voltage probe (Agilent 10076A) connected to an oscilloscope (Hewlett Packard 54602B).

The chamber is evacuated by a turbo-molecular and a rotary pump which provide a base pressure on the order of 10^{-5} Pa. Checks of the leak/de-gassing rate (measured by closing all input and output valves and monitoring the pressure rise rate in the chamber) resulted in a value between few times 10^{-5} and 10^{-4} sccm. These leak rate and base pressure values guaranteed that reliable measurements can be taken even at the lowest oxygen content in the gas mixtures. The discharges are operated at pressures ranging from 3.5 to 10 Pa. The chamber is continuously supplied with argon and oxygen gases of purities 6.0 and 5.0, respectively. The argon supply is regulated by a flow controller, while oxygen is supplied through a sapphire-sealed variable leak valve. This method maintains the working pressure and reduces the impact of impurities. As small quantities of oxygen are required, a careful calibration of the gas dosing systems was carried out, measuring the inflow rates of the feed lines individually and combined.

In order to measure the densities of $1s_5$ and $1s_3$ at the center of the reactor, the TDLAS system (Toptica LD-0773-0075-DFB-1) is configured to measure the absorption of the Ar $1s_5 \rightarrow 2p_6$ and $1s_3 \rightarrow 2p_2$ transitions with central wavelengths of 772.376 nm and 772.421 nm, respectively. A periodic wavelength sweep is achieved by driving the laser head with a triangular current waveform with a frequency of 5 Hz. The laser beam is coupled into the optical fiber with an integrated beam splitter. 90% of the laser power is directed to the Fabry–Perot interferometer (FPI) which can monitor the wavelength variation of the laser with a 1 GHz free spectral range. The output of the FPI serves as a reference signal, connecting the variation of the laser diode current with the laser wavelength. The remaining 10% of the laser light is guided into the plasma reactor through a fiber collimator, passes through the plasma chamber at a point midway between the electrodes, and is detected by the photodetector (ThorLabs APD130A2/M) on the other side. The laser beam entering the plasma has a waist of about 1.5 mm and a power of the order of 0.1 mW. We have continuously monitored the absorption line shape during the measurements and have ensured that the detection system operated in the linear regime without saturation. The photodetector and the FPI are both connected to a PC-based oscilloscope (PicoScope6403B). The experiment is controlled and the raw data are pre-processed using a custom LabVIEW virtual instrument.

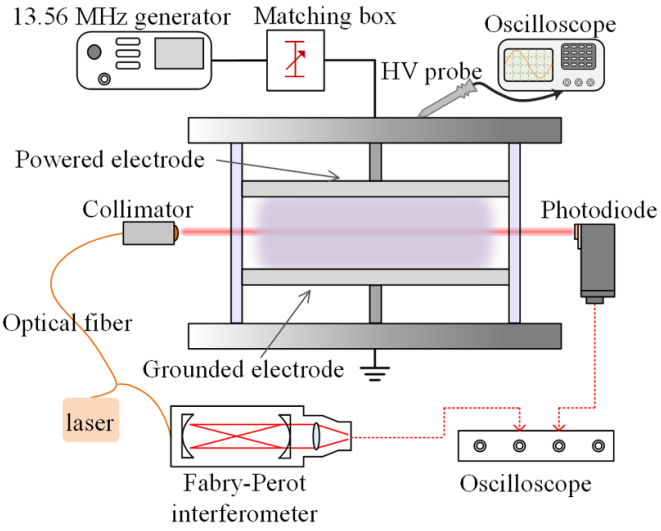

Figure 1. The scheme of the discharge setup and the TDLAS method.

2.2. Data processing

In order to obtain the metastable atom density based on the Beer–Lambert law, four light intensity (I) measurements were conducted with the plasma on and off (denoted as 'Pon/Poff') and the laser on and off (denoted as 'Lon/Loff') at each fixed sets of the discharge conditions to eliminate the effects of stray light and baseline variation. Using the measured intensities, the transmittance is calculated as:

$$T_\nu = \frac{I_{\mathrm{Pon}}^{\mathrm{Lon}}(\nu) - I_{\mathrm{Pon}}^{\mathrm{Loff}}(\nu)}{I_{\mathrm{Poff}}^{\mathrm{Lon}}(\nu) - I_{\mathrm{Poff}}^{\mathrm{Loff}}(\nu)} = e^{-k(\nu)l}, \tag{3}$$

where ν is the frequency of the laser and the sub- and superscripts correspond to the four data sets previously mentioned. The absorption length l is assumed to be the diameter of the electrodes, which is 14.0 cm in this case. Figure 2 shows exemplary measured absorption line shapes for selected mixing ratios at pressure $p = 5$ Pa and RF voltage $V_{\mathrm{pp}} = 300$ V.

Based on the absorption coefficient $k(\nu)$, the metastable density, n_{m}, can be obtained as follows:

$$k(\nu) = \frac{e^2}{4\epsilon_0 c m_{\mathrm{e}}} f n_{\mathrm{m}} F(\nu), \tag{4}$$

where e is the elementary charge, ϵ_0 is the vacuum permittivity, c is the speed of light, m_{e} is the electron mass, f is the oscillator strength set as 0.0278 for $1s_5$ and 0.314 for $1s_3$ [38]. $F(\nu)$ is the normalized function that represents the absorption line shape. Combining equations (3) and (4), the metastable

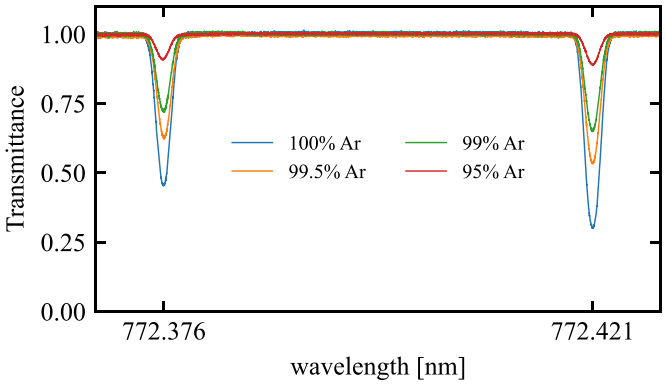

Figure 2. Exemplary measured absorption line shapes for selected mixing ratios at pressure $p = 5$ Pa and RF voltage $V_{pp} = 300$ V.

density is determined by the area, S, under the absorption line:

$$\int_0^\infty \ln\left(T_\nu^{-1}\right) \mathrm{d}\nu = S = \frac{e^2 l}{4\epsilon_0 c m_e} f n_m. \tag{5}$$

During the experimental procedure, the densities of metastable atoms were measured for a sequence of RF driving voltages for a given gas pressure. The reproducibility of the measurements was then verified by returning to the initial RF voltage and repeating the measurement. The results demonstrated that the deviation between the density values obtained through this method was below 10%.

3. Simulation method

The numerical calculations are based on two codes: a conventional one-dimensional PIC/MCC code and a Diffusion-Reaction-Radiation (DRR) code. Unlike in [11], where an iterative solution of the PIC/MCC and DRR modules was used for a pure Ar plasma, in the present case only a 'uni-directional' PIC/MCC → DRR coupling is employed due to the very high computational requirement of solving the two codes iteratively for the Ar/O_2 gas mixture. The reason for the latter stems from the long convergence time for the electronegative plasma where the balance of the negative ions, defined by the attachment and recombination processes, establishes on a long time scale. The uni-directional coupling is made possible by the fact that at low pressures the electron energy probability function (EEPF) does not change significantly due to the presence of stepwise and superelastic collisions, as shown in [11] for pressures up to ≈10 Pa.

The objective of the PIC/MCC code is to compute the spatial and temporal evolution of the relevant species present in Ar/O_2 mixtures and to output the rates of electron impact excitation of GS Ar atoms to all excited levels once the convergence has been achieved. Subsequently, the DRR code will utilize the excitation rates as source terms to solve the balance equations for Ar excited levels, thereby obtaining the desired metastable density distributions. These balance equations also include the rates of additional processes: stepwise excitation and ionization, as well as superelastic processes whose rates are computed using the spatially resolved EEPF provided by the PIC/MCC code, as well as the rates of the radiative transitions.

Details about the two parts of the computational framework are discussed in the following subsections.

3.1. The PIC/MCC code

The 1d3v electrostatic PIC/MCC code (named *PICit!*) was developed for the purpose of modeling geometrically symmetric CCPs in a variety of gases and gas mixtures [36, 39, 40]. In the present study, the trajectories of charged particles, including e^-, Ar^+ , O_2^+ , and O^- ions are traced. Here, due to the reason that the density of O_2^- ions is noticeably lower than that of O^- ions at low pressures [41], only O^- ions are taken into account for negative ions. Additionally, the density distribution of $O_2(a^1\Delta_g)$ metastable oxygen molecules is computed. The oxygen metastable molecule plays a crucial role in the loss of negative oxygen ions (O^-) and is indispensable for an accurate calculation of the negative ion density, as evidenced in [42]. The aforementioned particle species are subject to a total of 67 collision processes.

In the case of e^- + Ar collisions, the BSR cross section database [43] in LxCat [44] is utilized, including 31 excitation channels in addition to ionization and elastic collisions. For Ar^+ + Ar collisions, the isotropic and backward elastic scattering cross sections employed are those provided by Phelps [45]. The collisions between electrons and O_2 molecules include elastic scattering, rotational and vibrational excitation, metastable excitation, dissociative attachment, electronic excitation, dissociation, ionization, and dissociative excitation. Furthermore, the model incorporates charge transfer and isotropic elastic scattering for $Ar^+ + O_2$. For O_2^+ ions, charge exchange, isotropic elastic scattering with neutral particles and dissociative recombination are considered. O^- ions are involved in elastic scattering with neutral particles, detachment, mutual neutralization, and associative detachment. Further details regarding the processes involving oxygen can be found in [36] and are not repeated here. The above collision processes are listed in table 1.

While our oxygen discharge model, based on the processes listed in table 1 has been experimentally validated (through comparisons between experimental and computational results for the ion fluxes, discharge power, ion energy distribution functions at the electrodes [52], as well as spatio-temporal distributions of electron-impact excitation rates [40]), the chemistry of low-pressure oxygen plasmas is more complex [41] where a number of additional volume reactions (especially such that involve excited O atoms) and surface reactions may have a strong effect on the modeling results.

The computational domain is divided into $N_g = 512$ grid cells and the number of the time steps within an RF period is set to $N_t = 4000$, in order to resolve the plasma Debye length and the electron plasma oscillations, respectively [53]. The computational grid for the EEPF consists of $N_f = 60$ points which provides sufficient resolution for the DRR module. At the electrode boundaries, the ion-induced effective secondary electron yield is set as $\gamma = 0.07$ for the Ar^+ ions and $\gamma = 0.01$

Table 1. Particle processes considered in PIC/MCC code. Here, Ar^* denotes various excited levels of argon atoms.

Reaction	Process	Reference
$e^- + Ar \rightarrow e^- + Ar$	Elastic scattering	[43]
$e^- + Ar \rightarrow e^- + Ar^*$	Electronic excitation (to 31 levels)	[43]
$e^- + Ar \rightarrow 2e^- + Ar$	Ionization	[43]
$e^- + O_2 \rightarrow e^- + O_2$	Elastic scattering	[46]
$e^- + O_2(r=0) \rightarrow e^- + O_2(r>0)$	Rotational excitation	[47]
$e^- + O_2(v=0) \rightarrow e^- + O_2(v>0)$	Vibrational excitation	[47]
$e^- + O_2 \rightarrow e^- + O_2(a^1\Delta_g)$	Metastable excitation	[47]
$e^- + O_2 \rightarrow e^- + O_2(b^1\Sigma_g)$	Metastable excitation	[47]
$e^- + O_2 \rightarrow O + O^-$	Dissociative attachment	[47]
$e^- + O_2 \rightarrow e^- + O_2$	Electronic excitation	[47]
$e^- + O_2 \rightarrow O + O + e^-$	Dissociation	[47]
$e^- + O_2 \rightarrow O_2^+ + 2e^-$	Ionization	[48]
$e^- + O_2 \rightarrow O(3p^3P) + O + e^-$	Dissociative excitation	[47]
$e^- + O_2^+ \rightarrow O + O$	Dissociative recombination	[48]
$O_2^+ + O_2 \rightarrow O_2 + O_2^+$	Charge exchange	[48]
$O_2^+ + O_2 \rightarrow O_2^+ + O_2$	Elastic scattering	[48]
$O_2^+ + Ar \rightarrow O_2^+ + Ar$	Elastic scattering	[49]
$e^- + O^- \rightarrow 2e^- + O$	Electron impact detachment	[48]
$O^- + O_2 \rightarrow O^- + O_2$	Elastic scattering	[48]
$O^- + O_2 \rightarrow O + O_2 + e^-$	Detachment	[48]
$O^- + O_2^+ \rightarrow O + O_2$	Mutual neutralization	[48]
$O^- + O_2(a^1\Delta_g) \rightarrow O_3 + e^-$	Associative detachment	[50]
$O^- + Ar \rightarrow O^- + Ar$	Elastic scattering	[49]
$Ar^+ + Ar \rightarrow Ar^+ + Ar$	Elastic scattering	[45]
$Ar^+ + O_2 \rightarrow Ar + O_2^+$	Charge exchange	[51]
$Ar^+ + O_2 \rightarrow Ar^+ + O_2$	Elastic scattering	[49]
$Ar^+ + O^- \rightarrow O + Ar$	Mutual neutralization	[48]
$O_2(a^1\Delta_g) + \text{wall} \rightarrow \text{wall}$	Recombination ($\alpha = 8 \times 10^{-4}$)	[36]
$Ar^+ + \text{wall} \rightarrow \text{wall} + e^-$	Secondary electron emission ($\gamma = 0.07$)	[20]
$O_2^+ + \text{wall} \rightarrow \text{wall} + e^-$	Secondary electron emission ($\gamma = 0.01$)	[36]
$e^- + \text{wall} \rightarrow \text{wall} + e^-$	Reflection ($r = 0.7$)	[20]

for the O_2^+ ions while the effective electron reflection coefficient is set to $r = 0.7$ based on the findings of [20] .

3.2. The DRR code

The DRR code is designed to solve the balance equations for the density distributions of Ar atoms in 30 excited levels (Rydberg level excluded), including Ar $1s_5$ and $1s_3$ atoms, whose densities in the discharge center can be compared to experimental data. Due to the differing lifetimes and reaction processes of the various excited levels, these are divided into two groups with slightly different calculation methods.

Firstly, the densities of Ar atoms above the 1s levels are calculated. The sources of these levels consist of direct electron-impact excitation of the GS atoms (S_{GS}) and from other excited levels (S_{EI}), as well as radiation from higher levels (S_{rad}). Except that S_{GS} is input directly from PIC/MCC results, the other two source terms need calculation in DRR code. The losses are mainly due to radiation to lower levels and to a smaller extent to superelastic collisions. Given the short life of these levels, diffusion is not considered, and the balance equation for levels above 2p can be written as follows, with losses on the left hand side and sources on the right hand side:

$$\left(k_e n_e + \sum_i A_i \eta_i\right) n_{exc} = S_{GS} + S_{EI} + S_{rad}, \tag{6}$$

and for 2p levels:

$$\left(k_e n_e + \sum_i A_i \eta_i + k_Q n_{Ar}\right) n_{2p} = S_{GS} + S_{EI} + S_{rad}, \tag{7}$$

where k_e and n_e represent the electron-impact de-excitation rate coefficient and the electron density, respectively, while A_i and η_i stand for the Einstein coefficient and the escape factor [54, 55] of radiation to level i. Quenching by neutral Ar atoms is considered for 2p levels with the quenching rate coefficient k_Q [56, 57] and GS Ar atom density n_{Ar}. The electron impact rate coefficients are obtained based on the cross sections ($\sigma(E)$) and the EEPF $g_E(E)$ by the formula

$$k_e = \int_{E_{th}}^{\infty} \sigma(E) \sqrt{\frac{2E}{m_e}} \sqrt{E} g_E(E)\, dE. \quad (8)$$

The EEPF is, as already mentioned, obtained in the PIC/MCC simulation and is normalized as $\int \sqrt{E} g_E(E) dE = 1$. The cross sections of electron impact collision are taken from BSR database [43], which includes stepwise excitation processes. The cross sections of the reverse processes, i.e. of the superelastic collisions are obtained using the principle of detailed balance [58].

Subsequently, the density distributions of 1s levels are calculated by solving the diffusion equations:

$$-D\frac{\partial^2 n_{1s}}{\partial x^2} + \left(k_e n_e + 2k_p n_{1s} + \sum_i A_i \eta_i + k_Q n_{O_2} + \nu\right) n_{1s} = S_{GS} + S_{EI} + S_{rad} + S_{cas}, \quad (9)$$

where D is the diffusion coefficient of argon atoms, k_Q is the oxygen quenching rate coefficient and n_{O_2} is the density of O_2 molecules. Quenching by oxygen molecules is included for $1s_5$ and $1s_3$ levels with coefficients $k_{Q5} = 2.1 \times 10^{-10}\,cm^3\ s^{-1}$ and $k_{Q3} = 2.4 \times 10^{-10}\,cm^3\ s^{-1}$, respectively [59]. In fact, it is not only oxygen molecules that react with argon metastable atoms; oxygen atoms can also quench them. The rate was measured by King *et al* [60]. The investigations reported in [14, 32] concluded that the contribution of oxygen atoms to the total quenching rate is two orders of magnitude lower than that of the molecules. Therefore, it is reasonable to exclude the effect of oxygen atoms in this work.

Although the numerical model is one-dimensional in space, we have included the radial diffusion losses of the Ar excited atoms in order to more closely approximate the experimental conditions. The characteristic radial loss rate is represented by the loss frequency ν, with the following form [18]:

$$\nu = \frac{D}{(R/2.405)^2} \quad (10)$$

where R stands for the radius of the cylindrical experimental chamber. The boundary condition for equation (9) is

$$-D\frac{\partial n_{1s}}{\partial x} = \frac{\xi}{2(2-\xi)} n_{1s} \bar{v}, \quad (11)$$

where ξ is the recombination coefficient at the electrode set to be 0.5 [1] and $\bar{v}$ is the mean velocity of the neutral Ar species.

For the 1s levels, the source terms are similar to that of 2p levels, with the exception of the additional cascade sources originating from Rydberg levels. In [11], these higher levels were found to be subject to significant excitation by electron-impact collisions of GS Ar atoms, and the absence of radiation treatment for these levels was identified as a shortcoming of the model. In this study, we attempt to incorporate the influence of these highly excited levels by distributing their excitation rate in proportion to the total transition rates from the 2p levels to the 1s levels. Consequently, the cascade source terms of the four 1s levels are defined as

$$S^i_{cas} = \frac{S^i_{rad}}{\sum_i S^i_{rad}} \cdot S^{Ryd}_{GS} \quad (12)$$

where i represents a certain 1s level and S^{Ryd}_{GS} stands for the GS excitation rate to Rydberg levels.

Furthermore, the pooling ionization for the 1s levels is also considered by introducing the collision rate coefficient k_p.

Indeed, when calculating the source and loss terms in equations (7) and (9), the densities of the excited levels are required for parameters such as escape factors and electron impact rates as source terms. Therefore, the computation of density distributions is iterated until the relative differences of all local densities before and after the update are less than 10^{-6}.

4. Results

The following section presents the central Ar metastable atom densities obtained from simulations and experiments, along with an analysis of the relevant processes. For discharges in pure Ar, the data are analyzed as a function of the gas pressure, p, and the peak-to-peak RF voltage, V_{pp}. For Ar/O_2 mixtures, the O_2 concentration in the working gas is also varied from 0.5% to 10%.

4.1. Discharges in argon

Figure 3 depicts the comparison of the experimental and computational results for the densities of the two argon metastable species, $1s_5$ and $1s_3$. As illustrated in the figure, the density of the Ar atoms in both metastable levels increases with rising pressure and voltage, but reaches a saturation point at higher voltages, i.e. $V_{pp} > 200$ V. The experimental data are well reproduced by the simulations, concerning both the trends and the absolute values. In general, the density difference, between experiment and simulation, of the $1s_5$ density is smaller compared to that of the $1s_3$ level. The ratio of the simulation to the experimental values exhibits a maximum at $p = 10$ Pa and minimum at $p = 3.5$ Pa, with the values of 1.6 and 0.6, respectively.

The underlying causes of these discrepancies at the lowest and highest pressures are distinct. At the lowest pressure, the discharge operates almost at its limit, due to the less frequent collisions. As observed in the experiments, the plasma at $p < 3$ Pa, can only be operated following ignition at a higher pressure. It is reasonable to conclude that when the plasma approaches the edge of stable operation, even slight perturbations can induce significant changes in density. As for higher pressure, our present model gradually loses its accuracy without the feedback of metastable interactions to the PIC/MCC module. As indicated in [11], when the pressure of $p > 10$ Pa, the EEPF exhibits differences in the presence or absence of metastable levels in the simulation.

The density of metastable atoms is determined by the equilibrium between a number of elementary processes. For purposes of illustration, we will consider the case with $p = 5$ Pa and $V_{pp} = 300$ V as an example. The distributions of the species e^-, Ar^+, Ar $1s_5$ and $1s_3$ densities and process rates for the $1s_5$ metastable level are shown in figure 4. All the density profiles of the species are symmetric and reach the maximum at

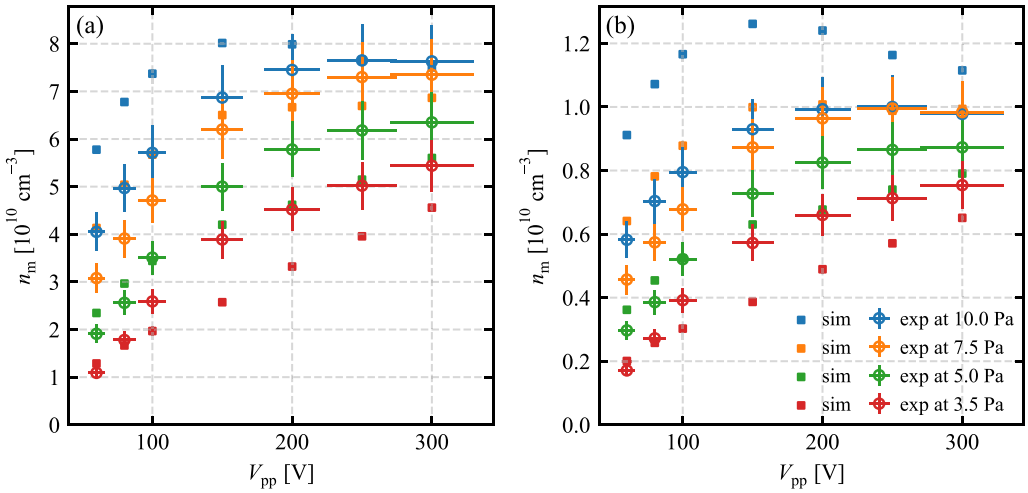

Figure 3. The central density of (a) $1s_5$ and (b) $1s_3$ atoms obtained from simulations ('sim') and experiments ('exp') for different pressures and voltages.

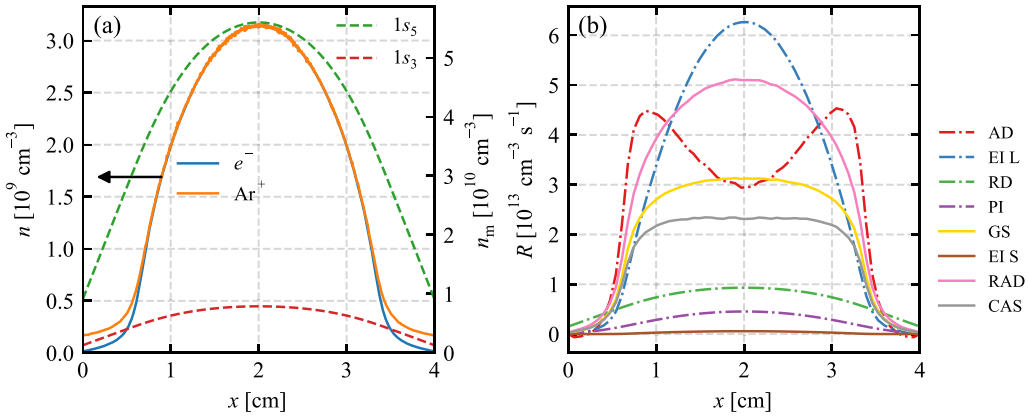

Figure 4. The spatial distribution of (a) density and (b) reaction rates involving the metastable Ar $1s_5$ level, at a pressure of $p = 5$ Pa and RF peak-to-peak amplitude of $V_{pp} = 300$ V in pure argon. Abbreviations used in the legend are resolved in table 2. In (b) the loss terms are presented in dash-dotted lines while sources are in solid lines.

the center. The densities of the metastable species are about one order of magnitude higher than those of the charged particles due to the lower energy threshold of excitation as compared to ionization, with a slightly different shape near the boundaries, which is caused by the fact that the motion of the charged particles is dictated by the sheath electric field, while neutral transport proceeds via diffusion.

Figure 4(b) illustrates the distribution of the rates of population and de-population processes involving the metastable $1s_5$ level. Note, that the abbreviations corresponding to these processes are listed in table 2. At the conditions under consideration, the dominant source and loss processes for Ar $1s_5$ are radiation from the 2p levels and stepwise electron impact excitation to other excited levels. It is expected that the contribution of each process to metastable density will vary with pressure and voltage. For instance, at lower pressures, diffusion will be more significant, whereas particle collisions will become more important as the pressure increases.

Table 2. Abbreviations for processes involving the Ar $1s_5$ state considered in this work.

Abbreviation	Process
AD	Axial diffusion
EI L	Electron impact loss
RD	Radial diffusion
PI	Pooling ionization
O_2	Quenching by oxygen molecules
GS	Ground state excitation
EI S	Electron impact source
RAD	Radiation contribution
CAS	Cascade contribution

4.2. Argon/oxygen mixtures

Figure 5 illustrates the changes in the plasma composition (charged particle densities) and the densities of the Ar metastable atoms as a function of increasing O_2 concentration

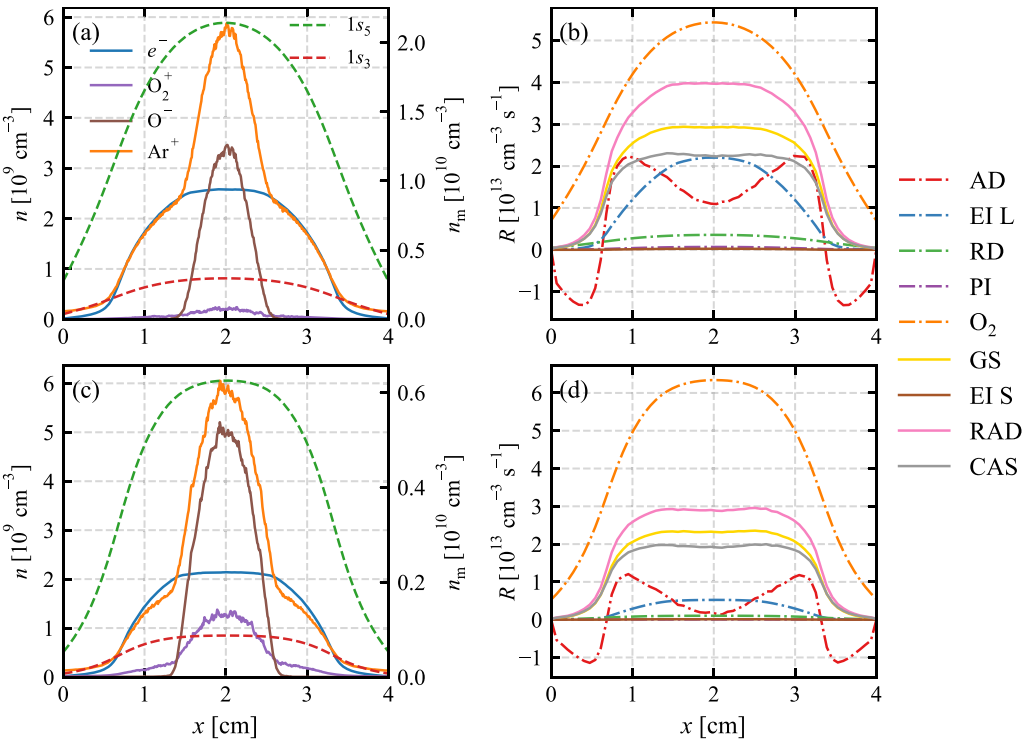

Figure 5. The distribution of (a), (c) the densities and (b), (d) reaction rates involving $1s_5$, where discharge conditions and legends are the same as in figure 4 except 'O_2' for oxygen quenching. The oxygen content is 1% (a), (b) and 4% (c), (d).

(panels (a), (c)) and the rates of the elementary processes that influence the density of the Ar $1s_5$ atoms (panels (b), (d)). Upon the introduction of 1% oxygen into the gas, the plasma bulk exhibits the emergence of O^- ions, with a density that is approximately equal to that of the electron density, as shown in figure 5(a). Therefore, the electronegativity in the bulk is on the order of unity. The concentration of O_2^+ ions is relatively low. In comparison to the discharge in pure Ar (see figure 4(a)), one can observe a reduction of the Ar metastable densities, by a factor of approximately 2.5. As the O_2 concentration is increased to 4%, the metastable densities decrease further, by a factor of approximately 3.7, in comparison to the case of 1% O_2 admixture, as shown in panel (c). Meanwhile, the discharge undergoes a shift towards greater electronegativity, with Ar^+ and O^- ions becoming the dominant plasma constituents in the bulk. The greater electronegativity not only reduces the Ar_m densities, but also alters their central distributions, which becomes flatter as a result of the changed electron distribution. Regarding the rates that govern the $1s_5$ metastable atom density, the quenching process by O_2 molecules emerges as the predominant loss channel even at such a low oxygen content as 1%, as revealed in figure 5(b).

Based on the encouraging outcomes of the comparison between the measured and computed metastable atom densities observed in pure argon, an investigation into the quenching impact of O_2 on Ar_m atoms can be undertaken in gas mixture discharges. Good agreement between the computed and measured metastable atom densities is achieved again as shown in figure 6. It is important to note that the simulation and experimental data have been normalized to the values observed in pure argon, which allows for a clearer illustration of the density variation with increasing oxygen content. As a result of the large quenching rate coefficient with O_2 molecules, densities of both metastable states decline almost exponentially.

As with pure argon, the contribution of each process varies with pressure and oxygen ratio. In the range of pressures under consideration, quenching by O_2 accounts for more than half of the metastable loss, with the remainder attributable to the electron impact reactions, and small diffusion losses, as shown in figure 7. As the pressure increases, the proportion of oxygen quenching also rises due to the larger number of oxygen molecules. On the contrary, the axial diffusion term reduces gradually with increasing pressure and even changes from positive to negative as a loss term, corresponding to the inward diffusion of the species from the regions of their most significant creation near the sheath edges. The change in the three main source terms is relatively minor, with only the GS excitation rate continuously increasing.

A similar analysis involving various oxygen ratios is presented in figure 8. As the oxygen content of the gas increases, quenching by O_2 accounts for the majority of the loss of metastable atoms, reaching almost 100% at 10 Pa gas pressure. Concurrently, a reduction in electron density at the electronegative center of the plasma results in decreased electron impact rates, including GS excitation processes. Moreover, in response to the large quenching rate, the axial diffusion tendency in the bulk changes gradually, resulting in negative diffusion at the center with higher oxygen content.

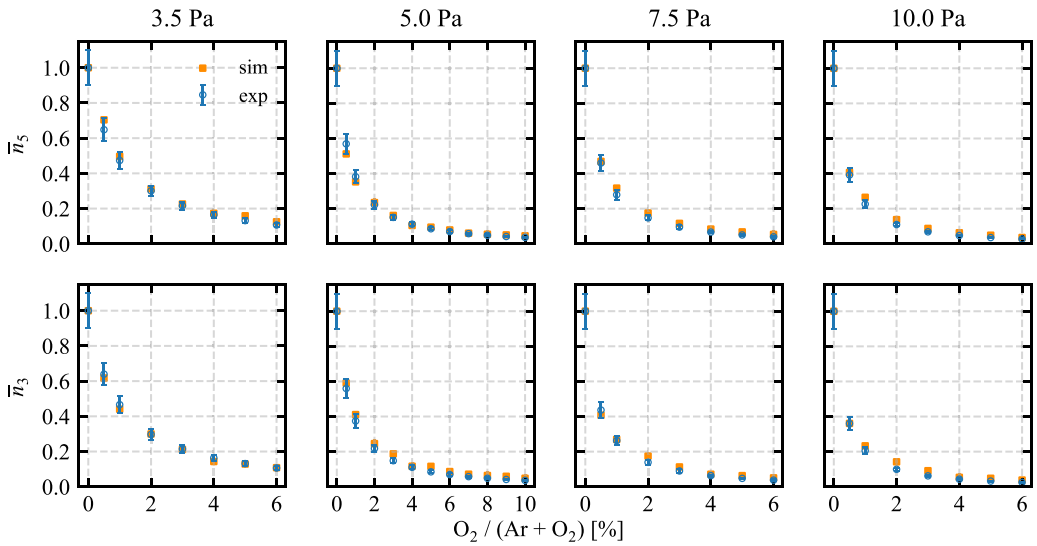

Figure 6. Normalized metastable densities $\overline{n} = n/n(0\%O_2)$ of $1s_5$ (top row) and $1s_3$ (bottom row) in mixtures with different oxygen ratios and pressures, for RF peak-to-peak voltage amplitude $V_{pp} = 300$ V.

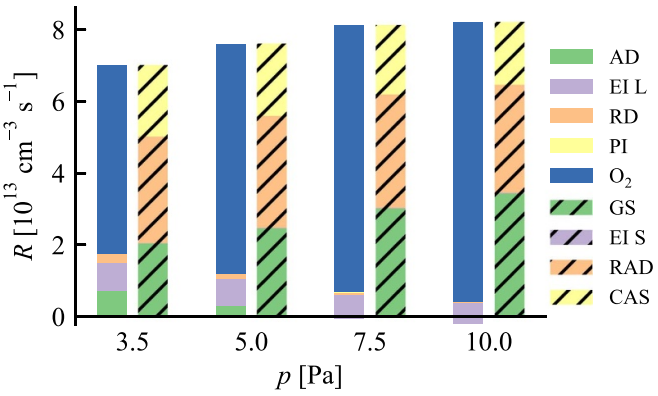

Figure 7. Central source (dashed bars) and loss (full bars) terms for $1s_5$ computed for different pressures, for 3% oxygen ratio and $V_{pp} = 300$ V.

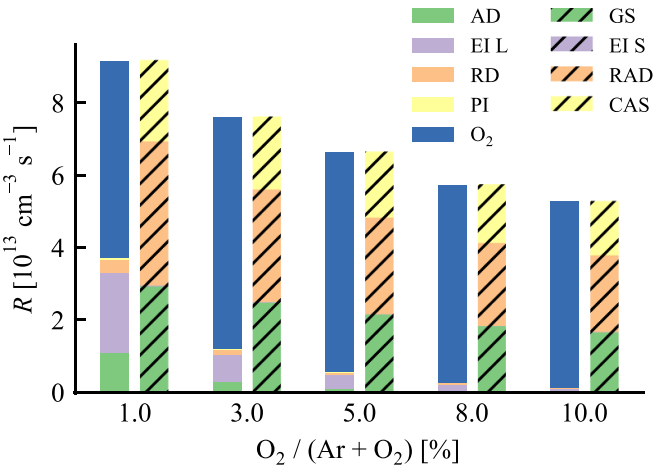

Figure 8. Central source (dashed bars) and loss (full bars) terms for $1s_5$ computed for different oxygen ratios, for $p = 5$ Pa and $V_{pp} = 300$ V.

5. Conclusions

In this study, the mechanism of quenching of metastable argon atoms by oxygen molecules in low pressure CCPs was investigated by a one-dimensional DRR code coupled with a PIC/MCC simulation of the Ar/O_2 RF plasmas. Experimental measurements for the densities of the Ar $1s_5$ and $1s_3$ metastable species were conducted to validate the simulation results. A good agreement between simulation and experimental results of metastable atom densities was achieved in both pure argon and argon/oxygen mixtures. This agreement serves to validate our proposed model for the production and destruction of argon metastable states at low pressures. Moreover, the results corroborate the validity of the oxygen quenching coefficients that have been widely utilized in the literature, as reported in [61]. Through simulations, details about process rates involving metastable atoms were presented, which are difficult to observe in experiments. The impact of oxygen admixture in the gas on argon metastable atoms is demonstrated to be considerable, resulting in a notable reduction in density and associated reaction rates. However, the current model is limited by a unidirectional data flow from the PIC/MCC model to the DRR code, which restricts its applicability to lower pressure conditions. To achieve a more comprehensive and extended numerical simulation, incorporating the iterative process between the two components represents a potential avenue for future exploration. However, this approach will be subject to significantly increased computational demand.

The substantial quenching of the excited Ar states in Ar/O_2 mixture CCPs also corroborates the rationale behind the satisfactory agreement between the measured and computed discharge characteristics, which was achieved in earlier works through a modeling approach that did not take into account the presence of the excited Ar levels [40].

Data availability statement

The data that support the findings of this study are available upon reasonable request from the authors.

Acknowledgments

This work was financially supported by China Scholarship Council (No. 202306210199) and the Hungarian National Office for Research, Development and Innovation (NKFIH) via the Grant K134462.

ORCID iDs

Lan-Yue Luo https://orcid.org/0009-0009-8522-8664
Zoltán Donkó https://orcid.org/0000-0003-1369-6150
Ranna Masheyeva https://orcid.org/0000-0002-6950-662X
Máté Vass https://orcid.org/0000-0001-9865-4982
He-Ping Li https://orcid.org/0000-0002-3149-757X
Peter Hartmann https://orcid.org/0000-0003-3572-1310

References

[1] Wen D Q, Krek J, Gudmundsson J T, Kawamura E, Lieberman M A and Verboncoeur J P 2021 *Plasma Sources Sci. Technol.* **30** 105009
[2] Makabe T 2019 *J. Phys. D: Appl. Phys.* **52** 213002
[3] Zhu H, Yao W and Li Z 2020 *Plasma Process. Polym.* **17** 1900271
[4] Yuan C, Zhou Z, Yao J, Bogdanov E, Kudryavtsev A and Rabadanov K 2019 *Plasma Sources Sci. Technol.* **28** 035017
[5] Roberto M, Smith H B and Verboncoeur J P 2003 *IEEE Trans. Plasma Sci.* **31** 1292–8
[6] Ferreira C, Loureiro J and Ricard A 1985 *J. Appl. Phys.* **57** 82–90
[7] Mushtaq S 2022 *J. Anal. At. Spectrom.* **37** 985–93
[8] Korolov I *et al* 2020 *J. Phys. D: Appl. Phys.* **53** 185201
[9] Yatom S, Chopra N, Kondeti S, Petrova T B, Raitses Y, Boris D R, Johnson M J and Walton S G 2023 *Plasma Sources Sci. Technol.* **32** 115005
[10] Ojha A, Pandey H and Pandey S 2023 *IEEE Trans. Plasma Sci.* **51** 3510–17
[11] Donkó Z, Hartmann P, Korolov I, Schulenberg D, Rohr S, Rauf S and Schulze J 2023 *Plasma Sources Sci. Technol.* **32** 065002
[12] Zheng B, Fu Y, Wen D Q, Wang K, Schuelke T and Fan Q H 2020 *J. Phys. D: Appl. Phys.* **53** 435201
[13] Lymberopoulos D P and Economou D J 1993 *J. Appl. Phys.* **73** 3668–79
[14] Rauf S and Kushner M J 1997 *J. Appl. Phys.* **82** 2805–13
[15] Sharma S, Sirse N, Turner M and Ellingboe A 2018 *Phys. Plasmas* **25** 063501
[16] Sung D, Wen L, Tak H, Lee H, Kim D and Yeom G 2022 *Materials* **15** 1300
[17] Napari M, Tarvainen O, Kinnunen S, Arstila K, Julin J, Fjellvåg Ø S, Weibye K, Nilsen O and Sajavaara T 2017 *J. Phys. D: Appl. Phys.* **50** 095201
[18] Lieberman M A and Lichtenberg A J 2005 *Principles of Plasma Discharges and Materials Processing* (Wiley) (https://doi.org/10.1002/0471724254)
[19] Han D M, Liu Y X, Gao F, Liu W Y, Xu J and Wang Y N 2018 *Chin. Phys.* B **27** 065202
[20] Schulenberg D A, Korolov I, Donkó Z, Derzsi A and Schulze J 2021 *Plasma Sources Sci. Technol.* **30** 105003
[21] Wen D Q, Krek J, Gudmundsson J T, Kawamura E, Lieberman M A and Verboncoeur J P 2022 *IEEE Trans. Plasma Sci.* **50** 2548–57
[22] Wen D Q, Krek J, Gudmundsson J T, Kawamura E, Lieberman M A, Zhang P and Verboncoeur J P 2023 *Plasma Sources Sci. Technol.* **32** 064001
[23] Gudmundsson J T, Krek J, Wen D Q, Kawamura E and Lieberman M 2022 *Plasma Sources Sci. Technol.* **30** 125011
[24] Bogaerts A and Gijbels R 1995 *Phys. Rev.* A **52** 3743
[25] Bogaerts A, Gijbels R and Vlcek J 1998 *J. Appl. Phys.* **84** 121–36
[26] Zhang Y R, Xu X and Wang Y N 2010 *Phys. Plasmas* **17** 033507
[27] Zhu X M and Pu Y K 2009 *J. Phys. D: Appl. Phys.* **43** 015204
[28] Gudmundsson J T and Thorsteinsson E 2007 *Plasma Sources Sci. Technol.* **16** 399
[29] McMillin B K and Zachariah M 1996 *J. Appl. Phys.* **79** 77–85
[30] Kitajima T, Nakano T and Makabe T 2006 *Appl. Phys. Lett.* **88** 091501
[31] Li S Z, Wu Q, Yan W, Wang D and Uhm H S 2011 *Phys. Plasmas* **18** 103502
[32] Bogaerts A 2009 *Spectrochim. Acta* B **64** 1266–79
[33] Sato T and Makabe T 2008 *J. Phys. D: Appl. Phys.* **41** 035211
[34] Hayashi Y, Hirao S, Zhang Y, Gans T, O'Connell D, Petrović Z L and Makabe T 2009 *J. Phys. D: Appl. Phys.* **42** 145206
[35] Fiebrandt M, Hillebrand B, Spiekermeier S, Bibinov N, Böke M and Awakowicz P 2017 *J. Phys. D: Appl. Phys.* **50** 355202
[36] Derzsi A, Hartmann P, Vass M, Horváth B, Gyulai M, Korolov I, Schulze J and Donkó Z 2022 *Plasma Sources Sci. Technol.* **31** 085009
[37] Horváth B, Derzsi A, Schulze J, Korolov I, Hartmann P and Donkó Z 2020 *Plasma Sources Sci. Technol.* **29** 055002
[38] Kramida A, Ralchenko Y and Reader J (NIST ASD Team) 2023 NIST atomic spectra database (ver. 5.11) (National Institute of Standards and Technology) (available at: https://physics.nist.gov/asd)
[39] Vass M, Wilczek S, Lafleur T, Brinkmann R P, Donkó Z and Schulze J 2021 *Plasma Sources Sci. Technol.* **30** 065015
[40] Derzsi A, Vass M, Masheyeva R, Horvath B, Donko Z and Hartmann P 2024 *Plasma Sources Sci. Technol.* **33** 025005
[41] Gudmundsson J, Kouznetsov I, Patel K and Lieberman M 2001 *J. Phys. D: Appl. Phys.* **34** 1100
[42] Gudmundsson J 2004 *J. Phys. D: Appl. Phys.* **37** 2073
[43] Zatsarinny O 2013 BSR database (available at: www.lxcat.net/BSR) (Accessed on 18 August 2022)
[44] Zatsarinny O and Bartschat K 2013 *J. Phys. B: At. Mol. Opt. Phys.* **46** 112001
[45] Phelps A V 1994 *J. Appl. Phys.* **76** 747–53
[46] Biagi S F 2012 Biagi-v89 database (available at: www.lxcat.net/Biagi) (Accessed on 25 November 2014)
[47] Vahedi V and Surendra M 1995 *Comput. Phys. Commun.* **87** 179–98
[48] Gudmundsson J T, Kawamura E and Lieberman M A 2013 *Plasma Sources Sci. Technol.* **22** 035011
[49] Langevin M 1905 Une formule fondamentale de théorie cinétique *Ann. Chim. Phys. Ser.* **5** 245–88
[50] Bronold F, Matyash K, Tskhakaya D, Schneider R and Fehske H 2007 *J. Phys. D: Appl. Phys.* **40** 6583
[51] Flesch G, Nourbakhsh S and Ng C 1990 *J. Chem. Phys.* **92** 3590–604
[52] Derzsi A, Bruneau B, Gibson A R, Johnson E, O'Connell D, Gans T, Booth J P and Donkó Z 2017 *Plasma Sources Sci. Technol.* **26** 034002

[53] Donkó Z, Derzsi A, Vass M, Horváth B, Wilczek S, Hartmann B and Hartmann P 2021 *Plasma Sources Sci. Technol.* **30** 095017
[54] Bhatia A and Kastner S 2000 *J. Quant. Spectrosc. Radiat. Transfer* **67** 55–63
[55] Siepa S, Danko S, Tsankov T V, Mussenbrock T and Czarnetzki U 2014 *J. Phys. D: Appl. Phys.* **47** 445201
[56] Sadeghi N, Setser D, Francis A, Czarnetzki U and Döbele H 2001 *J. Chem. Phys.* **115** 3144–54
[57] Horiguchi H, Chang R and Setser D 1981 *J. Chem. Phys.* **75** 1207–18
[58] Hartgers A, van Dijk J, Jonkers J and Van Der Mullen J 2001 *Comput. Phys. Commun.* **135** 199–218
[59] Velazco J, Kolts J and Setser D 1978 *J. Chem. Phys.* **69** 4357–73
[60] King D L, Piper L G and Setser D W 1977 *J. Chem. Soc., Faraday Trans. 2* **73** 177–200
[61] Piper L, Velazco J and Setser D 1973 *J. Chem. Phys.* **59** 3323–40